Institute of Paper Science and Technology
Atlanta, Georgia

IPST Technical Paper Series Number 806

Analysis of Turbulent Flow in the Converging Zone of a Headbox

V.S. Bandhakavi and C.K. Aidun

July 1999

Submitted to
1999 TAPPI Engineering/Process & Product Quality Conference
September 12-16
Anaheim, California

INSTITUTE OF PAPER SCIENCE AND TECHNOLOGY
PURPOSE AND MISSIONS

The Institute of Paper Science and Technology is an independent graduate school, research organization, and information center for science and technology mainly concerned with manufacture and uses of pulp, paper, paperboard, and other forest products and byproducts. Established in 1929, the Institute provides research and information services to the wood, fiber, and allied industries in a unique partnership between education and business. The Institute is supported by 52 North American companies. The purpose of the Institute is fulfilled through four missions, which are:

- to provide a multidisciplinary education to students who advance the science and technology of the industry and who rise into leadership positions within the industry;
- to conduct and foster research that creates knowledge to satisfy the technological needs of the industry;
- to serve as a key global resource for the acquisition, assessment, and dissemination of industry information, providing critically important information to decision-makers at all levels of the industry; and
- to aggressively seek out technological opportunities and facilitate the transfer and implementation of those technologies in collaboration with industry partners.

ACCREDITATION

The Institute of Paper Science and Technology is accredited by the Commission on Colleges of the Southern Association of Colleges and Schools to award the Master of Science and Doctor of Philosophy degrees.

NOTICE AND DISCLAIMER

The Institute of Paper Science and Technology (IPST) has provided a high standard of professional service and has put forth its best efforts within the time and funds available for this project. The information and conclusions are advisory and are intended only for internal use by any company who may receive this report. Each company must decide for itself the best approach to solving any problems it may have and how, or whether, this reported information should be considered in its approach.

IPST does not recommend particular products, procedures, materials, or service. These are included only in the interest of completeness within a laboratory context and budgetary constraint. Actual products, procedures, materials, and services used may differ and are peculiar to the operations of each company.

In no event shall IPST or its employees and agents have any obligation or liability for damages including, but not limited to, consequential damages arising out of or in connection with any company's use of or inability to use the reported information. IPST provides no warranty or guaranty of results.

Analysis of Turbulent Flow in the Converging Zone of a Headbox

Venkata S. Bandhakavi and Cyrus K. Aidun
Fluid Dynamics and Forming Research Unit, Institute of Paper Science and Technology
500 10th Street NW, Atlanta, GA 30318

Abstract

The tube block and the converging section are important design features of a headbox. The flow characteristics through these components have significant influence the forming jet hydrodynamics, which, in turn, influences the fundamental characteristics of the finished paper. Here, we present the numerical results of a three dimensional flow analysis inside a headbox, resulting from the interaction of tube jets in the converging zone of the headbox. For modeling turbulence, both RNG κ - ε model and Reynolds Stress Model (RSM) have been used to bring out the difference between the two. This parametric study mainly focuses on the effect of contraction ratio (CR), which is the ratio of inlet area of the headbox to the slice area. Results are presented in the form of machine direction (MD), cross direction (CD) components of velocity and also turbulent quantities at different sections along the length of the headbox for a given flow rate. The possible effects on the physical characteristics of the fiber network formation are discussed.

1. Introduction

This study is a follow-up to the author's previous article [1], in which, the small-scale nonuniformities in physical properties caused by the streaks on the forming table are attributed to the secondary flows induced by the tube jets inside the headbox. It has been observed that the interaction of jets from the tubes that feed the Headbox have a significant role in generating secondary flows in the headbox. Also, in [2], it was pointed out that two types of secondary flows are important. The first kind results from the flow retardation due to boundary layer formation at the side walls of a converging channel. The second kind results from anisotropy in turbulent Reynolds stress. The effect of anisotropic Reynolds stresses in the converging nozzle of a headbox and the inadequacy of the κ - ε model for this problem was also discussed in some detail in [2]. In this paper, a direct comparison between the RNG κ - ε model (which is an improved version of the standard κ - ε model), and a more appropriate turbulent model, namely, the Reynolds Stress Model (RSM) will be presented. A thorough understanding of the role of turbulence in the headbox and the impact of the mean secondary flows on fiber orientation and formation can be obtained only with appropriate turbulence models [2]. In a related study, Ullmar and Norman [3] experimentally investigated the effect of CR on fiber orientation. Their results indicate that the effect of CR is more significant on the fiber orientation than that of the flow velocity. The fibers have been found to be more strongly oriented in the MD for higher CR's. Hence, in this study, our objectives are: (1) to understand the flow structure in a headbox by making use of appropriate turbulence models; and (2) to study the effect of CR on the flow characteristics at the slice.

Although a number of studies appear in the literature on numerical and experimental investigations on converging-diverging nozzles (for example, [4-7]) with specific applications in aerospace/propulsion engineering, to date, there have been hardly any analyses of high speed incompressible turbulent flows in converging nozzles. One of the important physical aspects of flows through converging nozzles is the relaminarization of turbulent boundary layers, subjected to severe favorable pressure gradient. Launder [8], Moretti and Kays [9] were one of the first few to report reverse transition in accelerated incompressible turbulent boundary layers, even though instances of reverse transition have been mentioned in literature prior to them (for example, [10]). In their studies, the flows were subjected to large favorable pressure gradients associated with changes in Reynolds number. Badri Narayanan [11] experimentally investigated reverse transition from turbulent to laminar flow in a two-dimensional channel by artificially reducing the

Reynolds number below a certain value by widening the channel in the lateral direction. More recently, the laminarization of a fully turbulent flat plate boundary layer subjected to a favorable pressure gradient due to acceleration in a two dimensional contraction has been studied experimentally using constant temperature hot wire anemometry (CTA) by Tanaka and Yabuki [12] and Parsheh *et al* [13]. However, the Reynolds numbers in these experiments were of the order of 10^4. In our investigations, the Re is typically of the order of 3×10^5. Further, unlike in a simple contraction, where the flow only undergoes acceleration, in our studies, the flow initially undergoes sudden expansion as the jets from the tube bank enter the headbox. When the flow passes through the converging portion of the headbox , we expect the flow to undergo similar physics as described earlier. Even though, we do not expect the flow to relaminarize, in view of the high Re, and also, due to the short duration available for the flow inside the headbox before it reaches the slice, we do expect the turbulence levels to reduce as the flow accelerates.

In the following section, we briefly present the governing equations along with the turbulence models used in this study.

2. Governing Fluid Flow Equations and Turbulence Models

The momentum and mass conservation principles for an incompressible viscous fluid flow are given respectively, by

$$\rho\left(\frac{\partial \vec{u}}{\partial t}+\vec{u}\cdot\nabla\vec{u}\right)=-\nabla p+\rho\vec{g}+\nabla\cdot\tau \tag{1}$$

and

$$\nabla\cdot\vec{u}=0 \tag{2}$$

where

$\vec{u}=u_i=\left(u_x,u_y,u_z\right)=$ Instantaneous fluid velocity vector,

$p=$ Pressure,

$\vec{g}=$ Gravitational acceleration or body force per unit mass,

$\rho=$ Density, and

$\tau=2\mu D_{ij}=$ Fluid stress tensor, where D_{ij} is the strain tensor

$$D_{ij}=\tfrac{1}{2}\left(\frac{\partial u_i}{\partial x_j}+\frac{\partial u_j}{\partial x_i}\right) \tag{3}$$

For a Newtonian fluid with constant viscosity, the last term, representing the gradient of the stresses in the momentum equation is given by

$$\nabla\cdot\tau=\mu\nabla^2\vec{u} \tag{4}$$

where μ is the dynamic viscosity of the fluid.

In a turbulent flow, the velocity and pressure fields decompose into an ensemble mean (deterministic) and a randomly fluctuating (undeterministic) component respectively, as represented by

$$\vec{u}=\bar{\vec{u}}+\vec{u}' \tag{5}$$

$$p = \bar{p} + p' \tag{6}$$

In these equations, the *'overbar'* denotes the ensemble mean and the prime denotes the fluctuating components. After substituting Eqs. 5 and 6 into Eq. 1 and averaging Eq. 1 in time, the governing equations of a turbulent flow will now become

$$\rho\left(\frac{\partial \bar{\vec{u}}}{\partial t} + \bar{\vec{u}} \cdot \nabla \bar{\vec{u}}\right) = -\nabla \bar{p} + \rho \vec{g} + \nabla \cdot \hat{\tau} \tag{7}$$

and

$$\nabla \cdot \bar{\vec{u}} = 0 \tag{8}$$

In these equations, the stress tensor, $\hat{\tau}$, includes both the kinematic and the turbulent Reynolds stress tensors, such that

$$\nabla \cdot \hat{\tau} = \mu \nabla^2 \vec{u} + \nabla \cdot \tau^t \tag{9}$$

where

$$\tau_{ij}^{\ t} = -\rho \overline{u_i' u_j'} \tag{10}$$

The Reynolds stress tensor, τ^t, introduces additional unknowns for a turbulent flow problem governed by Eqs. 7 and 8. To describe the mean velocity and pressure fields, a closure equation is necessary to relate the components of the Reynolds stress tensor to the mean flow velocity or velocity gradients. Without a closure, one can only rely on Direct Numerical Simulation (DNS), which, in principle, solves the Navier-Stokes equations directly with sufficiently fine discretization to resolve the appropriate turbulent scales and obtains the instantaneous velocity and pressure fields. This approach demands a very fine spatial discretization with enormous computational cost. Hence, we must, for now, rely on methods that model the turbulent Reynolds stress terms presented in Eq.10. For the current analysis, the RNG κ-ε model and the Reynolds Stress Model (RSM), are used along with a segregated approach for solving the primitive variables. For these simulations, we use FLUENT, which is a Finite Volume Method (FVM) based commercially available software. Various details of the numerical methodology are explained in [14]. Here, we briefly, describe the RNG κ-ε model and the Reynolds Stress Model (RSM).

2.1. RNG κ-ε model

This model uses the Boussinesq hypothesis [15] to model the Reynolds stress tensor shown in Eq.10.

$$-\rho \overline{u_i' u_j'} = \mu_t\left(\frac{\partial \bar{u}_i}{\partial x_j} + \frac{\partial \bar{u}_j}{\partial x_i}\right) - \frac{2}{3}\left(\rho\kappa + \mu_t \frac{\partial \bar{u}_i}{\partial x_i}\right)\delta_{ij} \tag{11}$$

Here, the quantities u_i and u_j denote the averaged quantities. κ is the turbulent kinetic energy ($\frac{1}{2}\overline{u_i' u_i'}$) and δ_{ij} is the Kroneker delta. The standard κ-ε model which forms the basis for all the more advanced κ-ε models such as the RNG κ-ε model, makes use of the above hypothesis and has been widely used for various industrial problems since it was first proposed by Jones and Launder [16]. It is a semi-empirical model based on model transport equations for the turbulent kinetic energy (κ) and the rate of dissipation of turbulent kinetic energy (ε). The standard κ-ε model assumes the flow is fully turbulent and hence is valid only for such flows. The typical equations for κ and ε are given by

$$\rho\left(\frac{\partial \kappa}{\partial t} + \bar{\vec{u}} \cdot \nabla \kappa\right) = \nabla \cdot \left[\left(\mu + \frac{\mu_t}{\sigma_\kappa}\right)\nabla \kappa\right] + G_\kappa - \rho\varepsilon \tag{12}$$

$$\rho\left(\frac{\partial \varepsilon}{\partial t}+\vec{u}\cdot\nabla\varepsilon\right)=\nabla\cdot\left[\left(\mu+\frac{\mu_t}{\sigma_\varepsilon}\right)\nabla\varepsilon\right]+C_{1\varepsilon}\frac{\varepsilon}{\kappa}G_\kappa-C_{2\varepsilon}\rho\frac{\varepsilon^2}{\kappa} \tag{13}$$

In the above equations, contributions due to buoyancy terms and also due to fluctuating dilatation in compressible turbulence are neglected, as they are not relevant to the present problem. G_κ represents the generation (or production) term for the turbulent kinetic energy (κ), resulting from the mean velocity gradients. $C_{1\varepsilon}$ and $C_{2\varepsilon}$ are empirical constants and finally σ_κ and σ_ε are the effective turbulent Prandtl numbers for κ and ε respectively. The evaluation of the production term G_κ, and its significance in the accelerating flows is described shortly. In a standard κ-ε model, the eddy or turbulent viscosity μ_t is computed by combining κ and ε using the expression,

$$\mu_t=\rho C_\mu\frac{\kappa^2}{\varepsilon} \tag{14}$$

where C_μ is another empirical constant.

The RNG κ-ε model is derived from the instantaneous Navier-Stokes equations, using the "Renormalization Group (RNG) theory [17]. This leads to a model with constants different from those in the standard κ-ε model and also gives rise to additional terms in the equation for κ and ε. As a result it is expected to perform better for rapidly strained flows and flows involving significant swirl component. It also offers a somewhat more robust estimation for the effective viscosity (μ_t) by means of an analytically derived differential formula. The equations for κ and ε for the RNG κ-ε model are given by

$$\rho\left(\frac{\partial \kappa}{\partial t}+\vec{u}\cdot\nabla\kappa\right)=\nabla\cdot\left[\left(\alpha_\kappa\mu_{eff}\right)\nabla\kappa\right]+G_\kappa-\rho\varepsilon \tag{15}$$

$$\rho\left(\frac{\partial \varepsilon}{\partial t}+\vec{u}\cdot\nabla\varepsilon\right)=\nabla\cdot\left[\left(\alpha_\varepsilon\mu_{eff}\right)\nabla\varepsilon\right]+C_{1\varepsilon}\frac{\varepsilon}{\kappa}G_\kappa-C_{2\varepsilon}\rho\frac{\varepsilon^2}{\kappa}-R \tag{16}$$

Here, α_κ and α_ε, the inverse effective Prandtl numbers, are derived through the RNG theory. The **R** term in the equation for ε helps the RNG κ-ε model in yielding a more realistic turbulent viscosity in rapidly strained flows. The formula for α_κ, α_ε, the **R** term, and the differential formula for modeling the effective viscosity are described in detail in [18].

2.2. Turbulence production term in the κ-ε models

The term G_κ, representing the production of turbulent kinetic energy in Eqs. 12 and 15 is defined as

$$G_\kappa=-\rho\overline{u_i'u_j'}\frac{\partial\overline{u_j}}{\partial x_i} \tag{17}$$

This term is modeled using the Boussinesq hypothesis in the κ-ε models. This particular term is of great significance in the current study. As Hinze [15] explains, this term represents the work of deformation of the mean motion by the turbulent shear stresses and usually gives a positive contribution to the turbulent kinetic energy. Hence this term is also called the turbulence source term. Through extraction of energy from the mean motion, it transfers energy to the turbulent motion. This term however, yields interesting results when $i=j$ for flows accelerating in a particular direction. For a converging section, assuming x_1 to

be the predominant direction, we know that $\frac{\partial \overline{u_1}}{\partial x_1} > 0$. The turbulence production term, $-\rho \overline{u_1'^2} \frac{\partial \overline{u_1}}{\partial x_1}$, corresponding to this main motion is therefore negative. With the source term being negative, the turbulent kinetic energy (κ) decreases and the eddies dissipate rapidly through the nozzle. Conversely, in a flow with severe adverse pressure gradient (retarded flow in space), the tendency is to increase the turbulence. This term explains the reason for the relaminarization mentioned earlier and has been the topic of research in some of the articles cited. In the current work too, the reduction of turbulence is to be expected in the converging portion of the headbox. However, what makes the flow more complex in our study, (and so in a real headbox), is the fact that the flow initially undergoes a sudden expansion and hence an increase in the level of turbulence, before the flow actually starts experiencing the effect of contraction of the nozzle. Also, the length of the headbox in the axial direction is not enough for full laminarization of the flow. In addition, the outlet condition is also likely to affect the hydrodynamics of the flow, to some extent locally at the slice. In the next subsection, we briefly discuss the Reynolds stress Model (RSM), in which, the Reynolds stresses are not modeled as in the κ-ε models, but are evaluated from differential transport equations. Also, separate transport equations are solved for each of these stresses (thus accounting for the anisotropy of the turbulence). Hence RSM is inherently superior to the κ-ε models, which assume isotropic turbulence. (It may be recalled that, in an earlier section, anisotropy of turbulent Reynolds stresses is considered to be contributing to the secondary flows in a headbox forming jet).

2.3. Reynolds stress model (RSM)

This model solves transport equations for each of the terms in the Reynolds stress tensor [19,20]. An additional equation is also required for turbulent dissipation, ε. Thus the model requires 7 additional equations in three-dimensional computations as opposed to 2 additional equations in the κ-ε models. The individual Reynolds stresses are used to obtain the closure of the Reynolds averaged Navier Stokes equations shown in Eqs. 7 and 8. The derivation of the RSM involves multiplying the instantaneous momentum equation for each direction with the fluctuating velocity component in that direction and 'Reynolds-averaging' the resulting equation. A typical equation for the Reynolds stress can be represented as

$$\underbrace{\frac{\partial}{\partial t}\left(\rho \overline{u_i' u_j'}\right)}_{\text{Temporal Derivative}} + \underbrace{\frac{\partial}{\partial x_k}\left(\rho \overline{u_k u_i' u_j'}\right)}_{C_{ij} = \text{Turbulent Convection}} = \underbrace{D_{ij}^{T}}_{\text{Turbulent Diffusion}} + \underbrace{D_{ij}^{L}}_{\text{Molecular Diffusion}} + \underbrace{P_{ij}}_{\text{Stress Production}}$$

$$+ \underbrace{\phi_{ij}}_{\text{Pressure Strain}} - \underbrace{\varepsilon_{ij}}_{\text{Dissipation}} \tag{18}$$

Where,

$$D_{ij}^{T} = -\frac{\partial}{\partial x_k}\left[\rho \overline{u_i' u_j' u_k'} + \overline{p'\left(\delta_{kj} u_i' + \delta_{ik} u_j'\right)}\right] \tag{19}$$

$$D_{ij}^{L} = \frac{\partial}{\partial x_k}\left[\mu \frac{\partial}{\partial x_k}\left(\overline{u_i' u_j'}\right)\right] \tag{20}$$

$$P_{ij} = -\rho\left(\overline{u_i' u_k'} \frac{\partial \overline{u_j}}{\partial x_k} + \overline{u_j' u_k'} \frac{\partial \overline{u_i}}{\partial x_k}\right) \tag{21}$$

$$\phi_{ij} = \overline{p'\left(\frac{\partial u_i'}{\partial x_j} + \frac{\partial u_j'}{\partial x_i}\right)} \tag{22}$$

$$\varepsilon_{ij} = -2\mu\overline{\frac{\partial u_i'}{\partial x_k}\frac{\partial u_j'}{\partial x_k}} \tag{23}$$

It should be noted that some of the above terms contain additional unknown correlations , which, in turn, need to be either evaluated using higher order moments equations, or modeled in terms of calculable variables. The RSM employed here, is a second moment closure model and hence models the unknown correlations in the above equations instead of using additional equations. Thus, in Eqs.18-23, C_{ij}, D_{ij}^{L}, and P_{ij} , do not require any modeling, while D_{ij}^{T}, ϕ_{ij} and ε_{ij} need to be modeled to close the equations. The details for modeling these terms are explained in [19,20].

In the current study, we first use the RNG κ-ε model to examine the flow field for the three CR's. We, later, compare the results for CR=5.4 obtained with the RNG κ-ε model and the RSM to determine the relative accuracy of the two models. We, later, present the results for the three CR's using the RSM.

3. Details of Geometry, Mesh and Boundary Conditions

Fig.1 shows the geometry of the headbox considered in the current work. Only half of the geometry is considered in view of the symmetry of the flow configuration. The top and bottom sides are no slip walls, while the sides are symmetry boundaries. The fluid enters through the 3 circular inlets (semi-circular in the computations). The fluid in these computations is assumed to have the properties of water. Uniform inlet velocity profiles with zero CD and ZD components are applied at the inlet. At the outlet, zero normal and tangential components of stress tensor (commonly referred to as stress free boundary conditions) are applied. The mesh for this geometry consists of 204,611 cells and 219,600 points with 120 divisions in the X-direction (MD), 19 divisions in the Y-direction (CD), and 80 divisions in the Z-direction (ZD). All the computations have been carried out after proper non-dimensionalization.

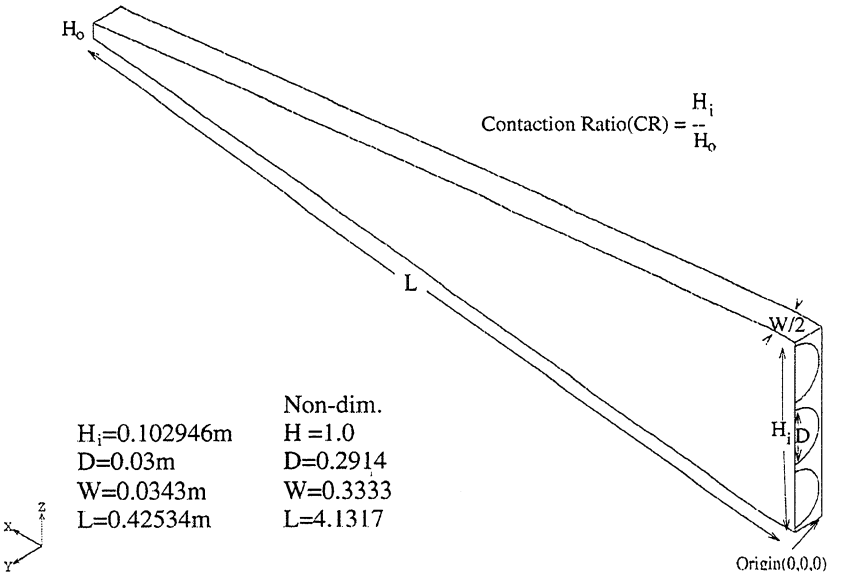

Figure 1: Geometry considered for the computation

The representative sections, where the results are presented are shown in Fig.2. The first of these sections is located at x = 0.1613 and marks the end of the non-converging section of the headbox. This section is very close to the inlet and the sudden expansion of the jets mostly takes place in this zone. The second section is located at approximately half the MD length of the headbox, and the third is located at the exit. The results are presented in the form of MD and CD components of velocity, and the turbulent kinetic energy at these 3 sections. Since each of these three sections has a different height in the Z-direction for each CR, while presenting the results along the vertical lines, we normalize the Z' (local coordinate system) with the height of the section.

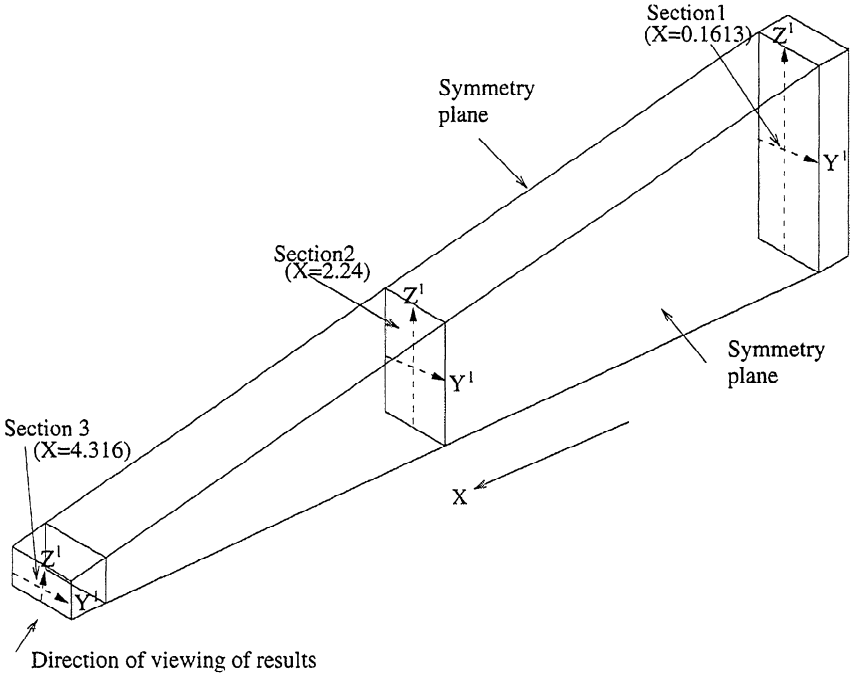

Figure 2: Sections where results are presented

It should be mentioned here that, on the symmetry planes shown in Fig.2, the CD velocity (U_y) is not identically equal to zero. The boundary condition only ensures that there is no flow across the cells located at these boundaries. Also in all the results presented, all the variables are plotted with their values at the cell centers and not at the nodes. Thus, in the plots of U_y, the values close to the symmetry side boundaries are not equal to zero. Also it should be mentioned that, while presenting the plots along the horizontal lines on the 3 sections, the coordinate system has been chosen such that 0 represents the left side boundary and 0.1667 represents the right side boundary with reference to the view direction depicted in Fig.2.

4. Results and Discussion

Numerical investigations are conducted for the following data shown in Table 1. The flow rates for all the three CR's is kept the same. This results in different mean flow velocities at the exit due to the difference in the slice areas. We first present the results for these cases using the RNG κ-ε model. This is followed by a comparison of the RNG κ-ε model and the RSM for CR=5.4 case to observe the relative accuracy of these two models. We then, present the results for the three CR's obtained from the RSM. Finally, we conclude with the interpretation of the results and their potential influence on the fiber orientation characteristics.

Table 1: Flow parameters considered for the three CR's

CR	Exit mean velocity (non-dimensional)	Mean flow rate/unit CD width (non-dimensional)
5.4	1.90 (≈ 4.75 m/s)	3.49 (≈ 0.093m^3/s/m)
8.0	2.77 (≈ 7.0 m/s)	
12.0	4.07 (≈ 10 m/s)	

4.1. RNG κ-ε Results for CR = 5.4, 8 and 12

As shown in Table 1, the flow rate is kept constant for the three CR's. This results in different flow velocities at the exit with CR=12 having the greatest mean flow velocity at the slice. Also, same value for turbulent kinetic energy (κ), corresponding to a turbulence intensity of 4 % has been applied at the inlet for the three CR's. The MD, and CD components of velocity (U_x, U_y), and the turbulent kinetic energy (κ), at the three sections shown in Fig.2 along the vertical and horizontal lines are shown in Figs. 3-11. The axial variation of all the three components of velocity (U_x , U_y , and U_z), and κ along a line joining the inlet mid-point to the outlet mid-point is shown in Fig. 12.

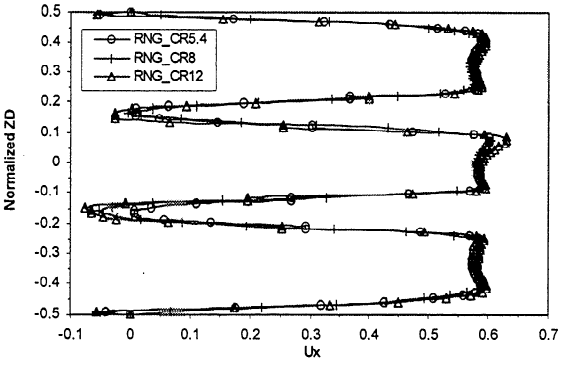

(a) MD velocity (Ux) along the vertical line @ section 1

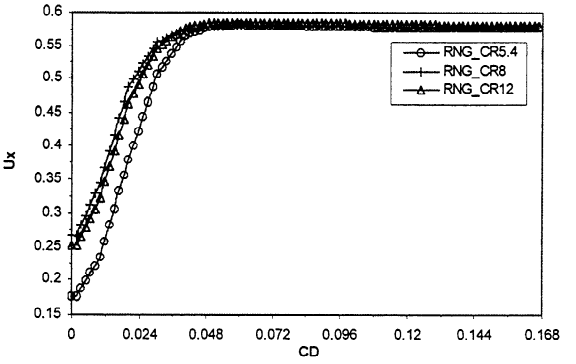

(b) MD velocity (Ux) along the horizontal line @ section 1

Figure 3 : MD velocity (U_x) for CR = 5.4, 8 and 12 at section 1 (RNG κ-ε model)

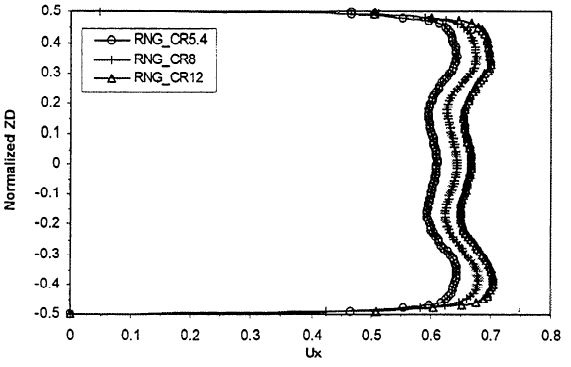

(a) MD velocity (Ux) along the vertical line @ section 2

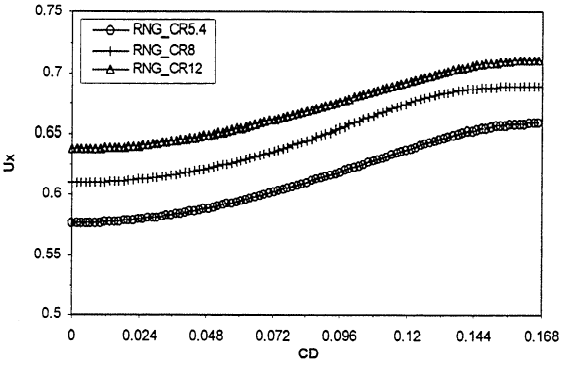

(b) MD velocity (Ux) along the horizontal line @ section 2

Figure 4 : MD velocity (U_x) for CR = 5.4, 8 and 12 at section 2 (RNG κ-ε model)

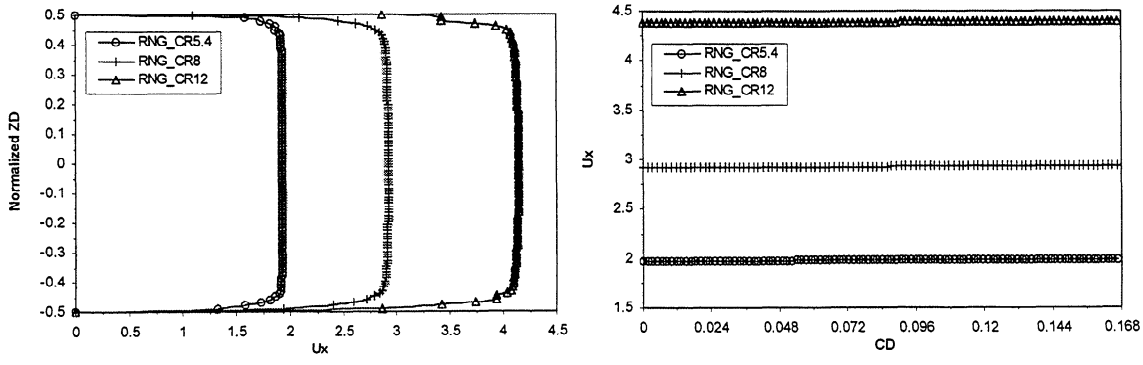

(a) MD velocity (Ux) along the vertical line @ section 3

(b) MD velocity (Ux) along the horizontal line @ section 3

Figure 5 : MD velocity (U_x) for CR = 5.4, 8 and 12 at section 3 (RNG κ-ε model)

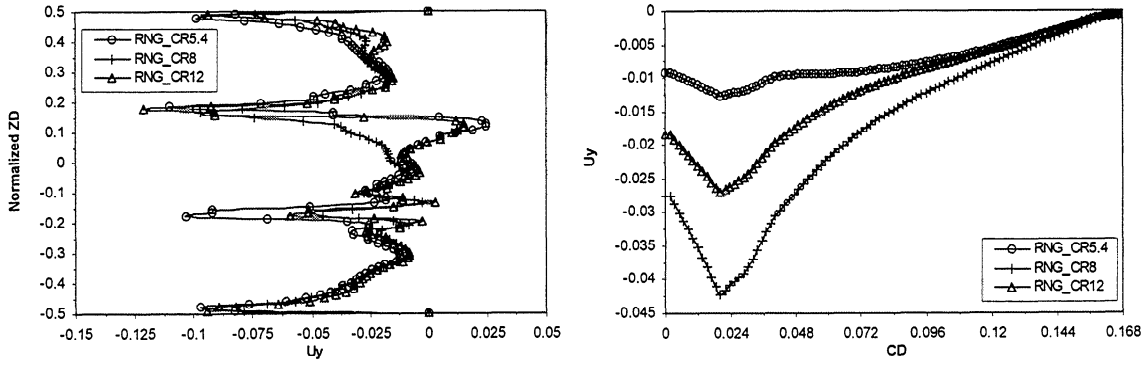

(a) CD velocity (Uy) along the vertical line @ section 1

(b) CD velocity (Uy) along the horizontal line @ section 1

Figure 6 : CD velocity (U_y) for CR = 5.4, 8 and 12 at section 1 (RNG κ-ε model)

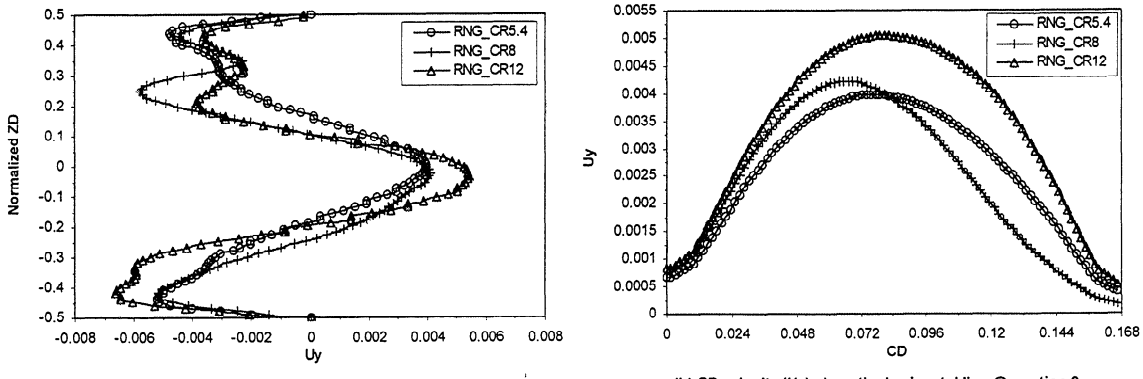

(a) CD velocity (Uy) along the vertical line @ section 2

(b) CD velocity (Uy) along the horizontal line @ section 2

Figure 7 : CD velocity (U_y) for CR = 5.4, 8 and 12 at section 2 (RNG κ-ε model)

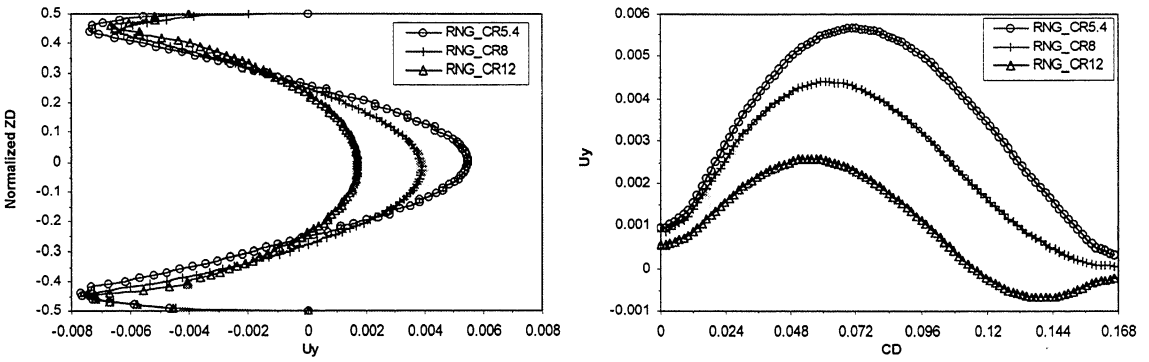

(a) CD velocity (Uy) along the vertical line @ section 3

(b) CD velocity (Uy) along the horizontal line @ section 3

Figure 8 : CD velocity (U_y) for CR = 5.4, 8 and 12 at section 3 (RNG κ-ε model)

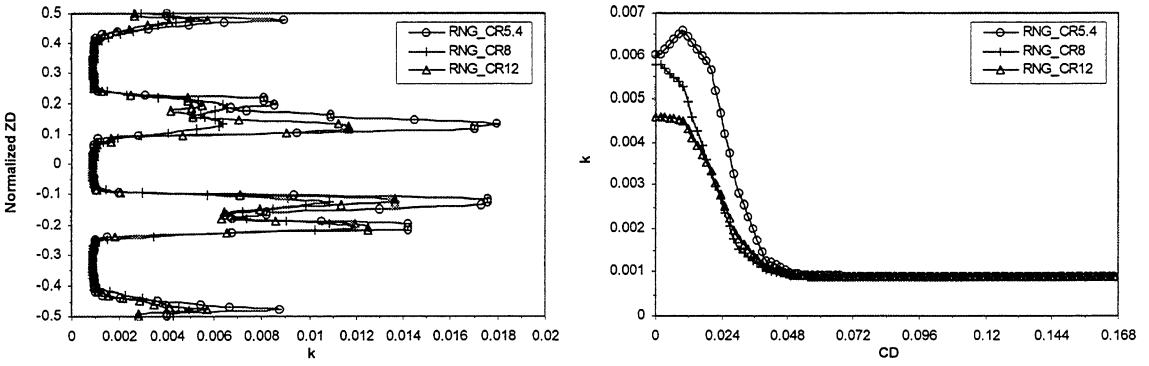

(a) Turb. KE (k) along the vertical line @ section 1

(b) Turb. KE (k) along the horizontal line @ section 1

Figure 9 : Turbulent kinetic energy (κ) for CR = 5.4, 8 and 12 at section 1 (RNG κ-ε model)

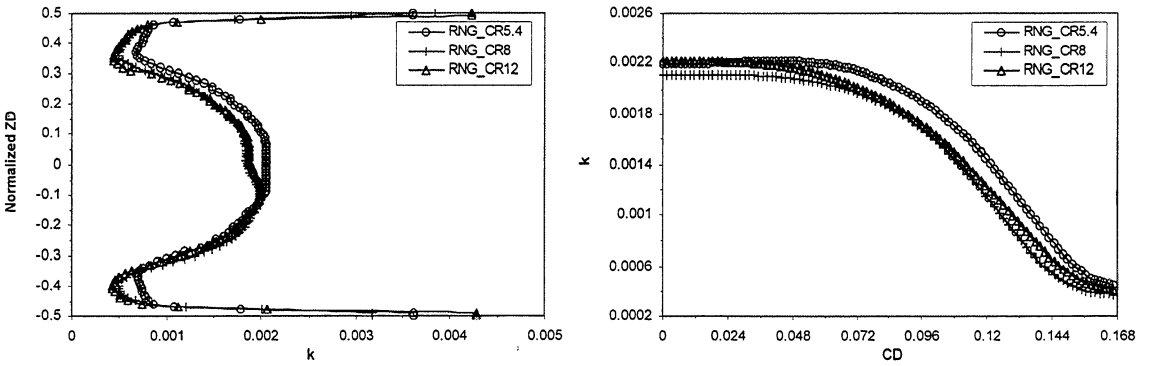

(a) Turb. KE (k) along the vertical line @ section 2

(b) Turb. KE (k) along the horizontal line @ section 2

Figure 10 : Turbulent kinetic energy (κ) for CR = 5.4, 8 and 12 at section 2 (RNG κ-ε model)

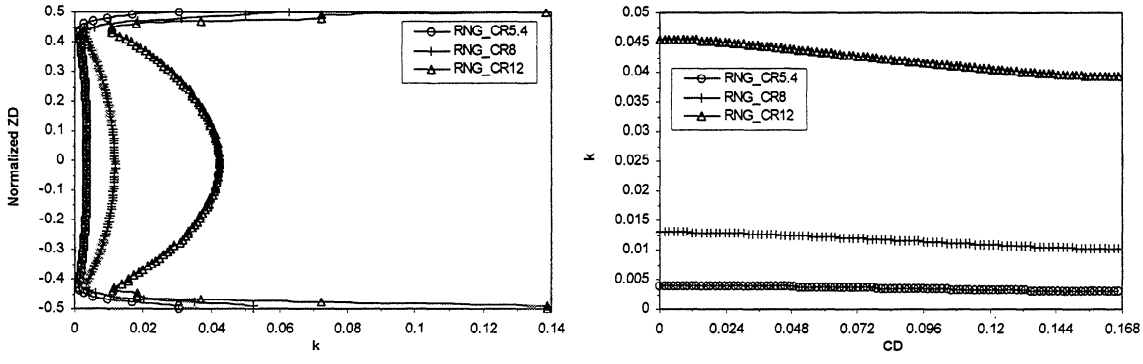

(a) Turb. KE (k) along the vertical line @ section 3

(b) Turb. KE (k) along the horizontal line @ section 3

Figure 11 : Turbulent kinetic energy (κ) for CR = 5.4, 8 and 12 at section 3 (RNG κ-ε model)

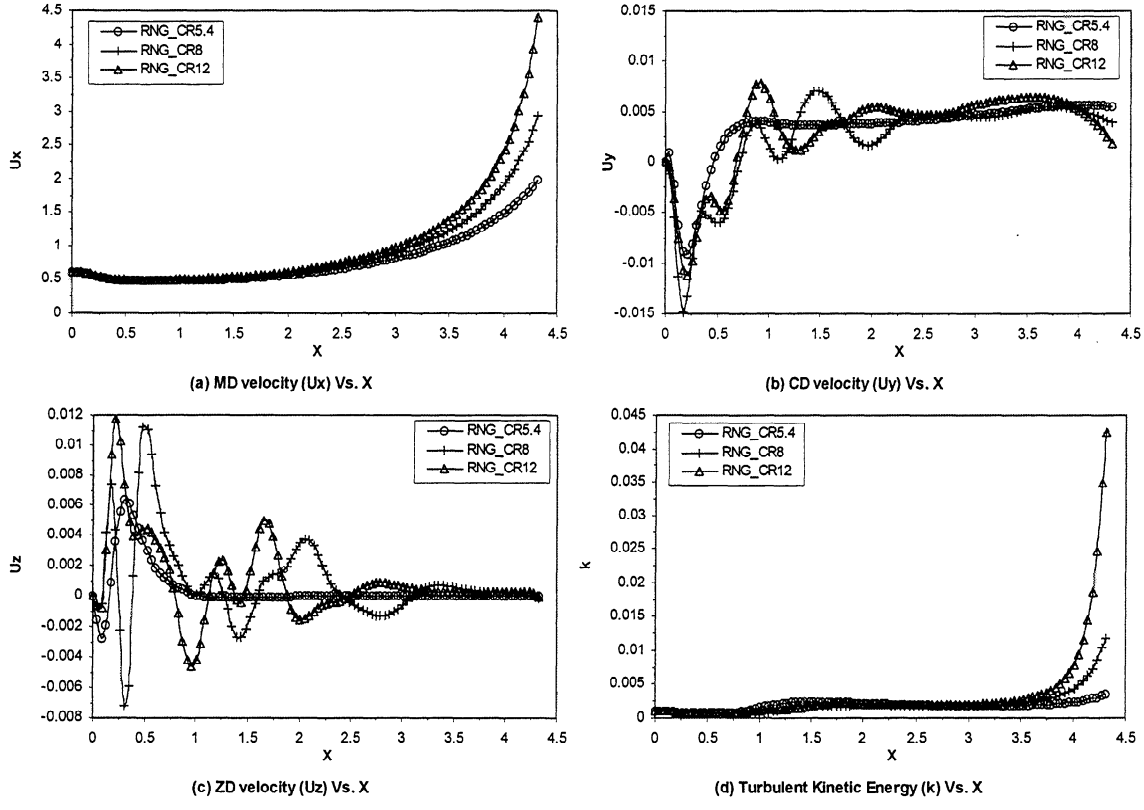

(a) MD velocity (Ux) Vs. X

(b) CD velocity (Uy) Vs. X

(c) ZD velocity (Uz) Vs. X

(d) Turbulent Kinetic Energy (k) Vs. X

Figure 12 : MD (U_x), CD (U_y Figure), and ZD (U_z) components of velocity, and turbulent kinetic energy (κ) along a line in the axial direction joining the mid-point of the inlet to the mid-point of the outlet.

Since the geometry has symmetry side boundary conditions and also is symmetric in the Z-direction, we would expect the CD and ZD components of velocity to vanish near section 3 or the slice (this, however, would not be true, for all inlet boundary conditions). However, near the inlet, the flow conditions are not uniform (the flow enters through 3 semi-circular pipes) in the CD. Thus larger variations in the CD are expected near section 1. From Figs. 3 – 12, we observe the following anomalies with respect to the flow field.:

1. From Fig.3 (b), we notice that the CD variation of U_x at section 1 for CR=5.4 falls below that for either CR=8 or CR=12. Since section 1 is at the end of the non-converging portion of the headbox, and is very close to the inlet, one would expect all the 3 curves to be very close.
2. The CD velocity (U_y) variation at section 1 for CR=8 from Fig.6 (b) is more pronounced than that for either CR=5.4 or CR=12.
3. Also, from Figs. 7 and 8, the CD velocity (U_y) components remain significant even at sections 2 and 3. Further, the CD component for CR=5.4 increases from section 2 to 3 which is contrary to the physics of the problem.
4. Similar observations have been made w.r.t. ZD component (U_z) , (the figures for which have not been presented here). One would expect U_z to be zero along the centerline in the horizontal direction. However, these are of the order of 1×10^{-3}, and may not be negligible.
5. Also, at the symmetry planes, one would expect U_y to be very nearly zero, but, once again they are significant (of the order of 1×10^{-3}).
6. The most serious drawback of this approach could be seen in the case of turbulent kinetic energy (κ) predictions from Figs.10 and 11, in which κ has significantly increased from section 2 to section 3 for the 3 CR's. Also the turbulent intensity for CR=12 is higher than that for CR=8 which, in turn, has higher turbulence intensity than CR=5.4, This clearly goes against the concept of relaminarization through attenuation of turbulence, which was discussed earlier (§ 2.2).
7. Finally from Fig. 12, we notice that the CD and ZD components of velocity undergo greater oscillations in the axial direction as CR increases, which is due to higher velocities as a result of contraction. (In general, the difficulty in obtaining convergence increases significantly with the CR). Also from κ variation, we notice that near the outlet, κ increases drastically (especially for higher CR's). This may be responsible for the odd behavior of κ from sections 2 to 3 described in the previous paragraph. Further tests are needed to find out whether this is due to the traction free boundary conditions or due to the physical reality of the situation. Some preliminary tests conducted in this direction will be discussed in a later subsection.

The results, obtained so far, prove the need to employ a more sophisticated model for turbulence. A number of reports appear in the literature demonstrating the superior performance of 'second moment closure models' *vis-à-vis* the κ-ε model (for example, [21,22]). One of the weaknesses of the κ-ε model is the isotropicity of the Boussinesq effective viscosity. Also, in practice, the turbulent shear stress is less directly connected with the mean velocity field than is required by the notion of a turbulent viscosity. Hence, in the next subsection, we present a comparison between the results obtained through the RNG κ-ε model and the Reynolds stress Model (RSM).

4.2 Comparison of RNG κ-ε model and RSM for CR = 5.4

Here, we chose CR=5.4 as a typical case for comparing the relative accuracy of RNG κ-ε model and RSM. We present the comparisons at sections 2 and 3 only. Figs.13-16 show the variation of MD, and CD components of velocity along the vertical and horizontal midlines, while Fig.17 shows their variation along the axial-midline of the geometry. From the figs. 13-14, one can notice that the MD velocity (U_x) predicted by the RSM is more uniform in the CD compared to the RNG κ-ε model. Since this problem is an axially dominant problem with no wall boundaries on the sides, the RSM predictions may be considered more accurate from these plots. Similarly from Figs. 15-16, CD velocity (U_y), is very close to zero along the horizontal midlines at both sections 2 and 3 with the RSM. Also notice, that the CD component reduces from section 2 to section 3 unlike the RNG κ-ε model predictions, in which the CD velocity (U_y) actually increases from section 2 to section 3. Also the profiles for ZD velocity (U_z) at sections 2 and 3 (these plots are not shown) prove that the RSM solution is superior to that given by the RNG κ-ε model.

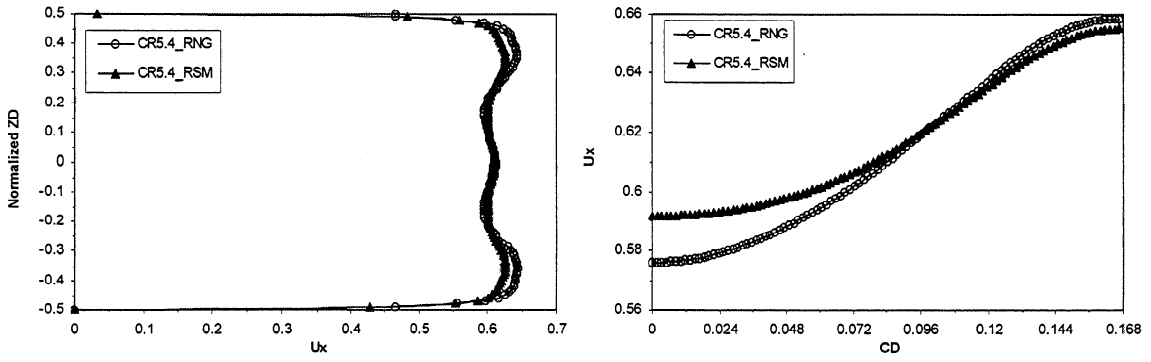

(a) Comparison of Ux along the vertical line @ section 2

(b) Comparison of Ux along the horizontal line @ section 2

Figure 13 : MD velocity (U_x) for CR = 5.4 at section 2 with RNG κ-ε model and the RSM

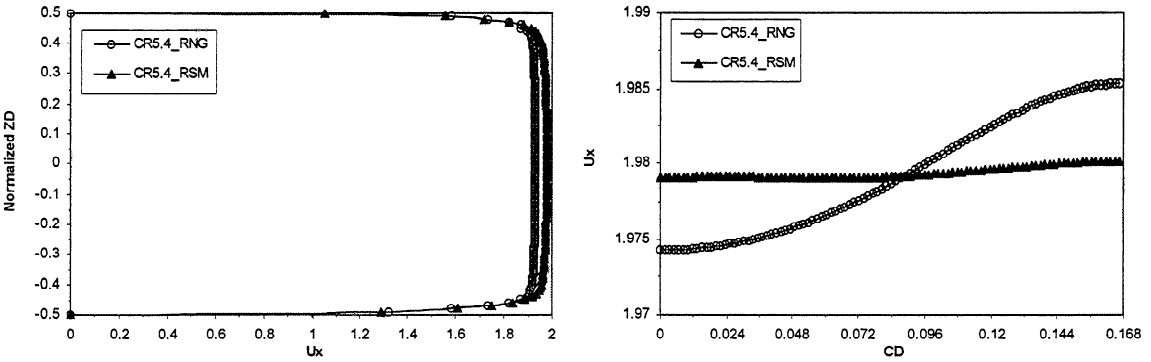

(a) Comparison of Ux along the vertical line @ section 3

(b) Comparison of Ux along the horizontal line @ section 3

Figure 14 : MD velocity (U_x) for CR = 5.4 at section 3 with RNG κ-ε model and the RSM

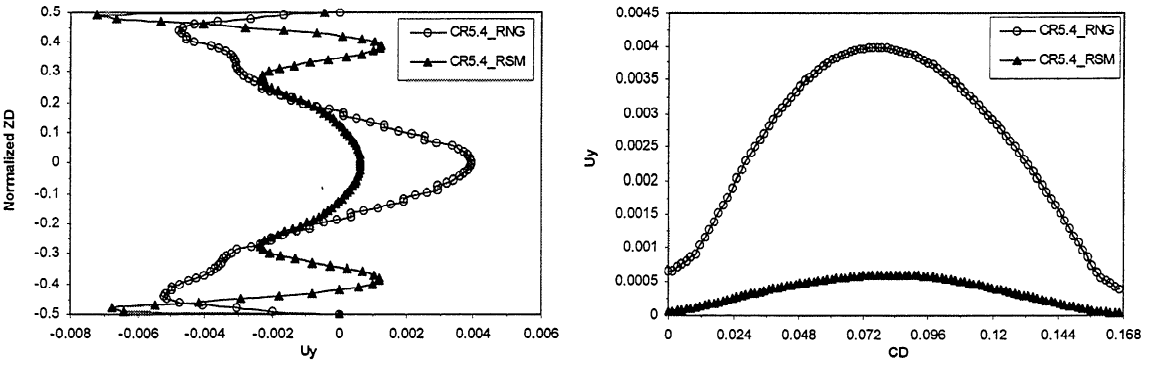

(a) Comparison of Uy along the vertical line @ section 2

(b) Comparison of Uy along the horizontal line @ section 2

Figure 15 : CD velocity (Uy) for CR=5.4 at section 2 with RNG κ-ε model and the RSM.

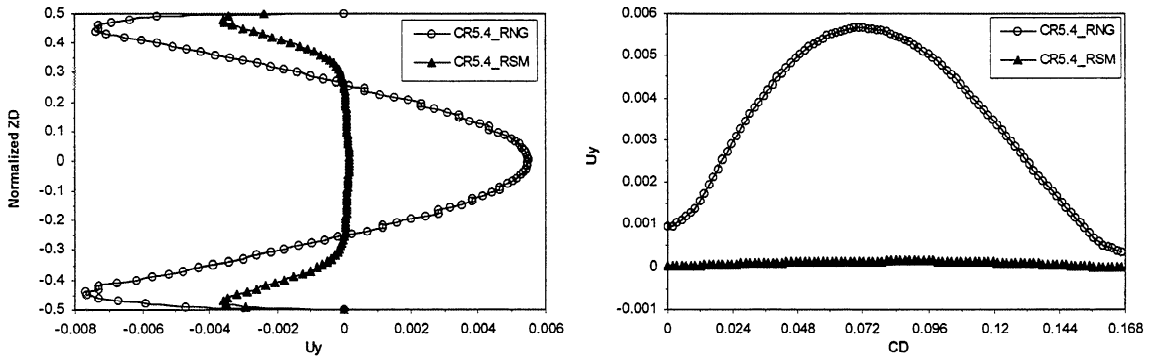

(a) Comparison of Uy along the vertical line @ section 3

(b) Comparison of Uy along the horizontal line @ section 3

Figure 16 : CD velocity (Uy) for CR=5.4 at section 3 with RNG κ-ε model and the RSM

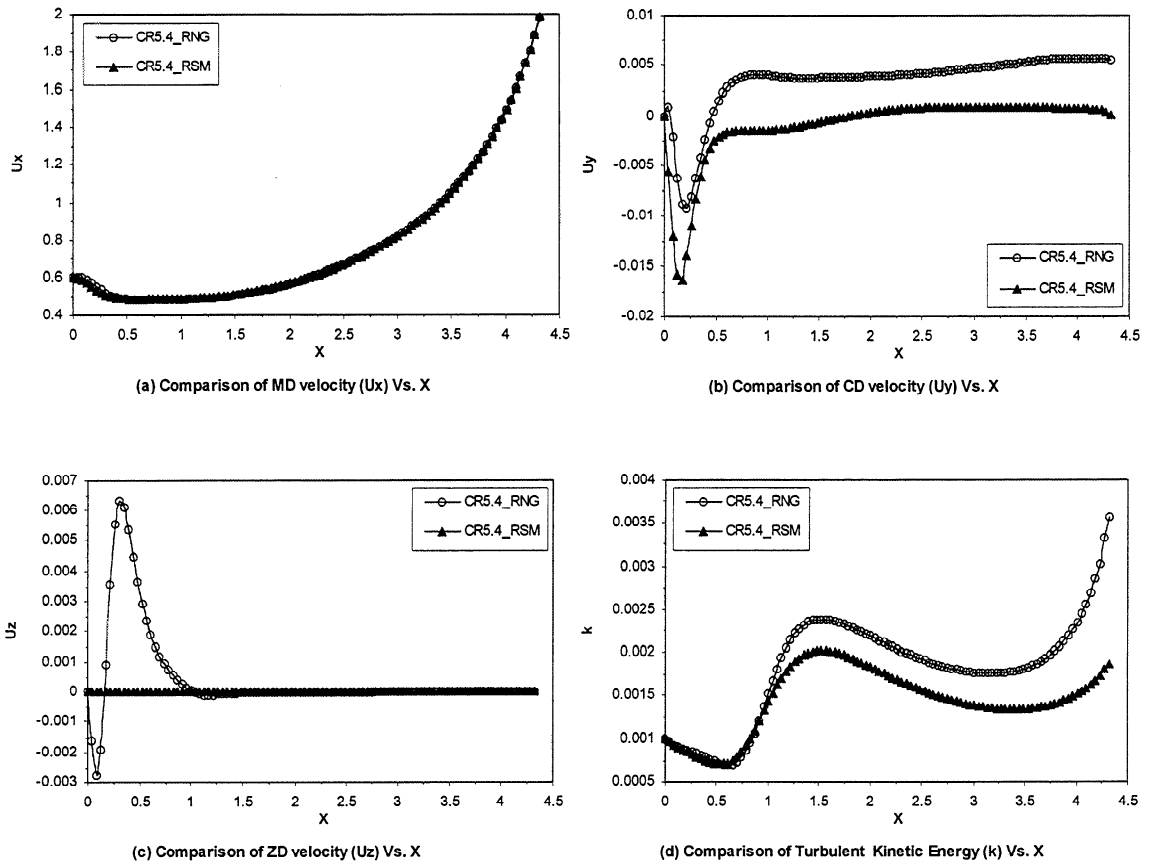

(a) Comparison of MD velocity (Ux) Vs. X

(b) Comparison of CD velocity (Uy) Vs. X

(c) Comparison of ZD velocity (Uz) Vs. X

(d) Comparison of Turbulent Kinetic Energy (k) Vs. X

Figure 17 : MD, CD, and ZD components of velocity, and turbulent kinetic energy along a line in the machine direction joining the inlet mid-point to the outlet mid-point for CR = 5.4 with the RNG κ-ε model and the RSM.

Fig. 17 also includes the axial variation of U_z and the turbulent kinetic energy (κ) as predicted from the RSM flow field compared with that from the RNG κ-ε model. Here too, the RSM performs better close to the outlet. Similar behavior is observed for CR=8 and 12 cases, the results for which are not presented here. In addition, the results with RSM exhibit fewer oscillations in the variation of Uy and Uz for all the three CR's. In the following subsection we present a comparison of the results with the RSM for the three CR's, *viz.,* 5.4, 8 and 12. Another significant advantage of the RSM can be realized, when we present the variation of individual Reynolds stresses, which describe the turbulence field more appropriately than a single scalar, κ.

4.3. Reynolds Stress Model (RSM) results for CR = 5.4, 8, and 12

The results presented in Figs. 18-21 are once again restricted to sections 2 and 3. These figures more or less follow the trends already described and are presented for the sake of completeness. They once again, serve to confirm the greater consistency in the RSM solutions compared to the RNG κ-ε solutions. Most of the focus, in this subsection, will be on different turbulent stress components as predicted by the RSM.

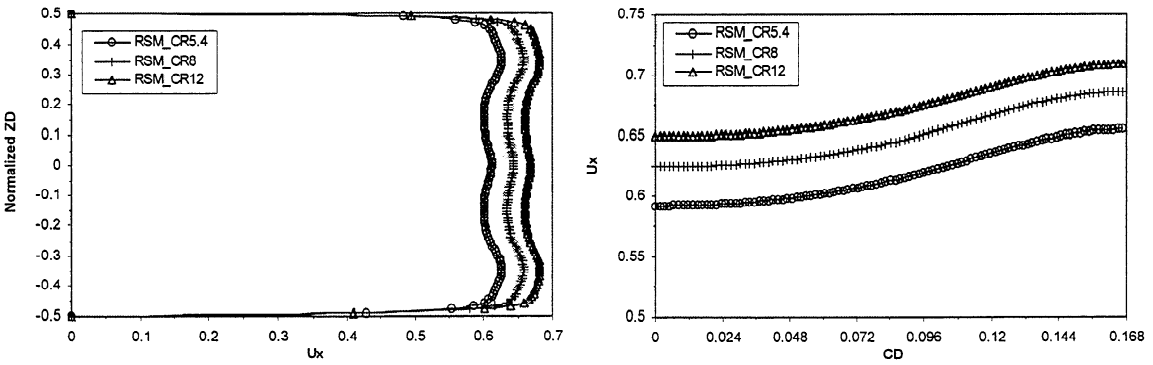

(a) MD velocity (Ux) along the vertical line @ section 2

(b) MD velocity (Ux) along the horizontal line @ section 2

Figure 18 : MD velocity (U_x) for CR = 5.4, 8 and 12 at section 2 (RSM)

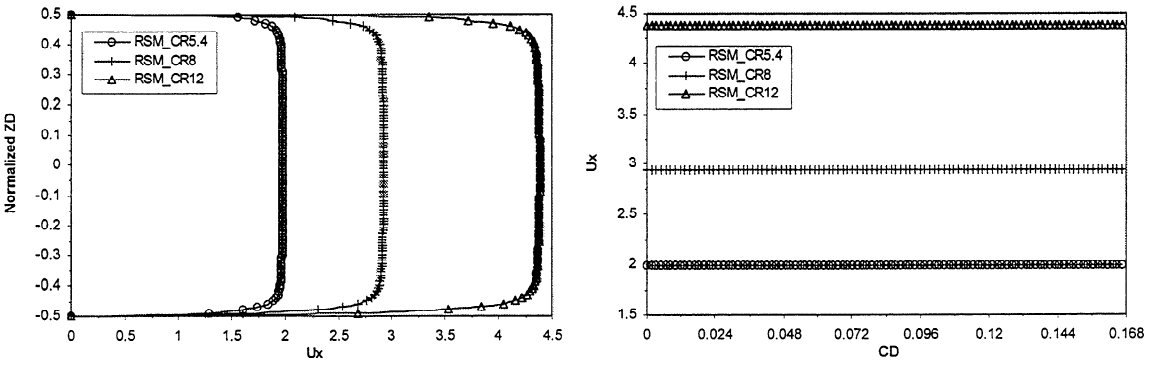

(a) MD velocity (Ux) along the vertical line @ section 3

(b) MD velocity (Ux) along the horizontal line @ section 3

Figure 19 : MD velocity (U_x) for CR = 5.4, 8 and 12 at section 3 (RSM)

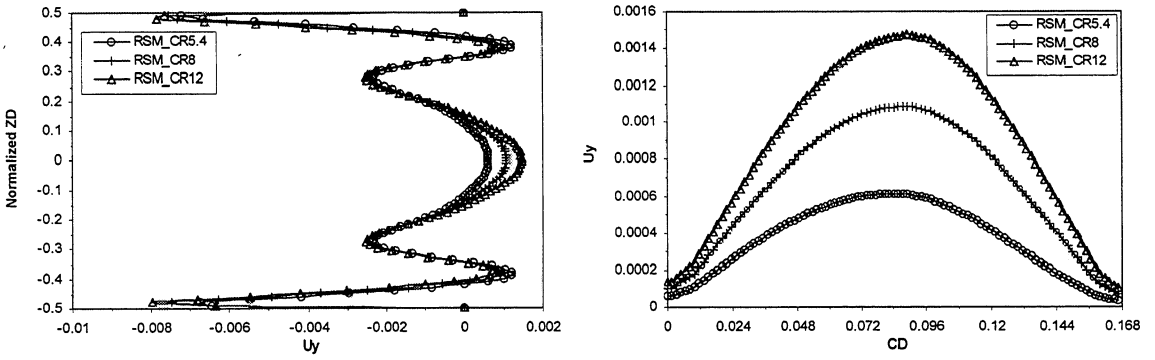

(a) CD velocity (Uy) along the vertical line @ section 2

(b) CD velocity (Uy) along the horizontal line @ section 2

Figure 20 : CD velocity (U_y) for CR = 5.4, 8 and 12 at section 2 (RSM)

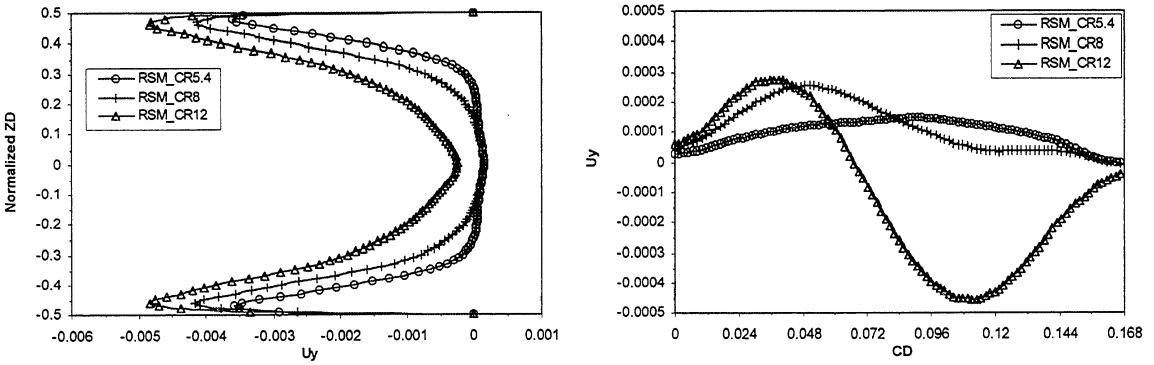

(a) CD velocity (Uy) along the vertical line @ section 3

(b) CD velocity (Uy) along the horizontal line @ section 3

Figure 21 : CD velocity (U_y) for CR= 5.4, 8 and 12 at section 3 (RSM)

Fig.22 shows the variation of significant Reynolds stresses in the axial direction along a line joining the inlet midpoint to the outlet midpoint. It should be mentioned here that the shear stress components involving the velocity fluctuations in the Z-direction (namely, $\rho\overline{u'w'}$ and $\rho\overline{v'w'}$) are negligible and hence are not shown in the Fig.22. From this figure, it is, at once, clear that different stress components increase or decrease in different ways, which indicates that the turbulence is not isotropic. This anisotropy in turbulence may produce (and influence) the secondary motion in the headbox in ways that a κ-ε model will not be able to predict. In this context, it is worth mentioning a discussion that Parsheh *et al.* [13] have presented. Their discussion deals with what are known as *'Prandtl's formulas'*, which imply that the longitudinal component of turbulence (u') diminishes on passing through a plane contraction, whereas the lateral components (v', w') grow. These changes are sharper for higher CR's. This sharp decrease of longitudinal and increase of lateral components causes the turbulence to become anisotropic. While these formulae may not apply exactly for all the geometries, they, in essence, imply that flows accelerating in particular directions may cause anisotropy of turbulence. In order to understand how the stresses vary in the current geometry, it is necessary to consider the contribution to the stress equations from the convective terms and the production terms. A detailed analysis of various terms (including the diffusion and dissipation terms) in different zones of the headbox will be presented in a future publication. Here, we briefly mention various significant terms in the later half of the headbox, where the flow is dominantly

accelerating along the contraction. These terms are presented in Table 2. In the first half of the headbox where the expansion and interaction of jets takes place, this analysis is more complex and more terms need to be considered.

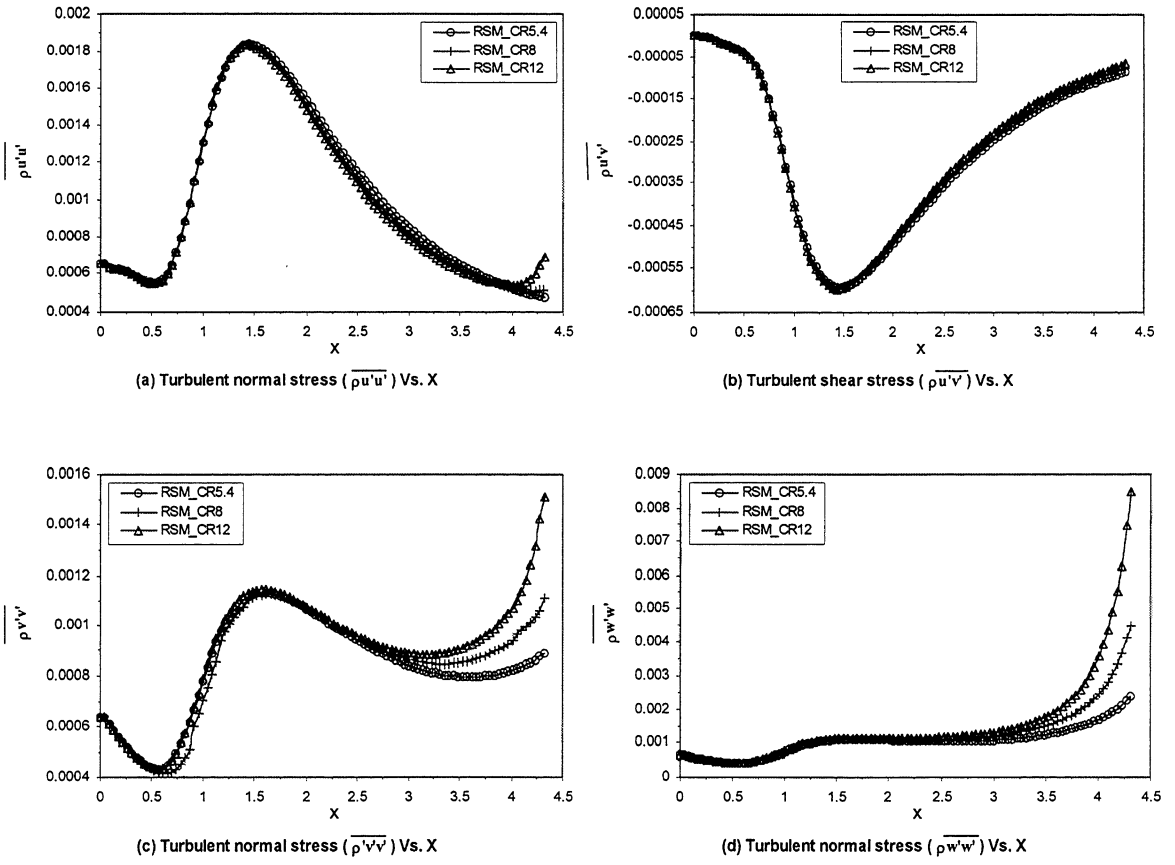

Figure 22 : Significant components of Reynolds stresses along the line joining the inlet midpoint to the outlet midpoint.

The significance of each of the terms shown in Table 2 is based on the mean flow acceleration patterns in the three directions. By plotting the various velocity gradients along the mid-axial line, one can qualitatively analyze how the different components of stress vary along the contraction. The estimation of the contribution from the convective terms in column 2 of Table 2 requires some additional computations. While the mean flow gradients largely dictate the overall orientation of the fibers, the small-scale velocity fluctuations (or in other words, the Reynolds stresses) will influence the fiber network orientation at smaller length scales. In the current headbox studies, it can be easily seen that the fiber orientation will be predominantly in the MD direction, and towards the center of the slice with the orientation being stronger with higher CR's. The strong MD and ZD gradients shown in Fig. 23 will support this view. It can be seen that these gradients are higher for higher CR's. The anisotropic turbulent stresses will influence the fiber network orientation either through extensional strain (in the case of turbulent normal stresses), or though shear deformation/rotation (in the case of turbulent shear stresses). Further studies of the relative strengths of the mean convective motion and the Reynolds stresses is needed to gain a better understanding of the fiber network orientation.

Table 2: Significant convective and stress production terms in the later half of the contraction

Reynolds stress	Significant convective terms	Significant stress production terms
$\rho\overline{u'^2}$	$\frac{\partial}{\partial x}\left(\bar{u}\rho\overline{u'^2}\right)+\frac{\partial}{\partial z}\left(\bar{w}\rho\overline{u'^2}\right)$	$\underbrace{-2\rho\overline{u'^2}\frac{\partial\bar{u}}{\partial x}}_{-ve} \underbrace{-2\rho\overline{u'v'}\frac{\partial\bar{u}}{\partial y}}_{\approx 0} \underbrace{-2\rho\overline{u'w'}\frac{\partial\bar{u}}{\partial z}}_{\approx 0}$
$\rho\overline{u'v'}$	$\frac{\partial}{\partial x}\left(\bar{u}\rho\overline{u'v'}\right)+\frac{\partial}{\partial z}\left(\bar{w}\rho\overline{u'v'}\right)$	$\underbrace{-\rho\overline{u'^2}\frac{\partial\bar{v}}{\partial x}}_{\approx 0} \underbrace{-\rho\overline{v'^2}\frac{\partial\bar{u}}{\partial y}}_{\approx 0} \underbrace{-\rho\overline{u'v'}\frac{\partial\bar{u}}{\partial x}}_{+ve}$ $\underbrace{-\rho\overline{u'v'}\frac{\partial\bar{v}}{\partial y}}_{\approx 0} \underbrace{-\rho\overline{u'w'}\frac{\partial\bar{v}}{\partial z}}_{\approx 0} \underbrace{-\rho\overline{v'w'}\frac{\partial\bar{u}}{\partial z}}_{\approx 0}$
$\rho\overline{v'^2}$	$\frac{\partial}{\partial x}\left(\bar{u}\rho\overline{v'^2}\right)+\frac{\partial}{\partial z}\left(\bar{w}\rho\overline{v'^2}\right)$	$\underbrace{-2\rho\overline{v'^2}\frac{\partial\bar{v}}{\partial y}}_{\approx 0} \underbrace{-2\rho\overline{u'v'}\frac{\partial\bar{v}}{\partial x}}_{\approx 0} \underbrace{-2\rho\overline{v'w'}\frac{\partial\bar{v}}{\partial z}}_{\approx 0}$
$\rho\overline{w'^2}$	$\frac{\partial}{\partial x}\left(\bar{u}\rho\overline{w'^2}\right)+\frac{\partial}{\partial z}\left(\bar{w}\rho\overline{w'^2}\right)$	$\underbrace{-2\rho\overline{w'^2}\frac{\partial\bar{w}}{\partial z}}_{+ve} \underbrace{-2\rho\overline{v'w'}\frac{\partial\bar{w}}{\partial y}}_{\approx 0} \underbrace{-2\rho\overline{u'w'}\frac{\partial\bar{w}}{\partial x}}_{\approx 0}$

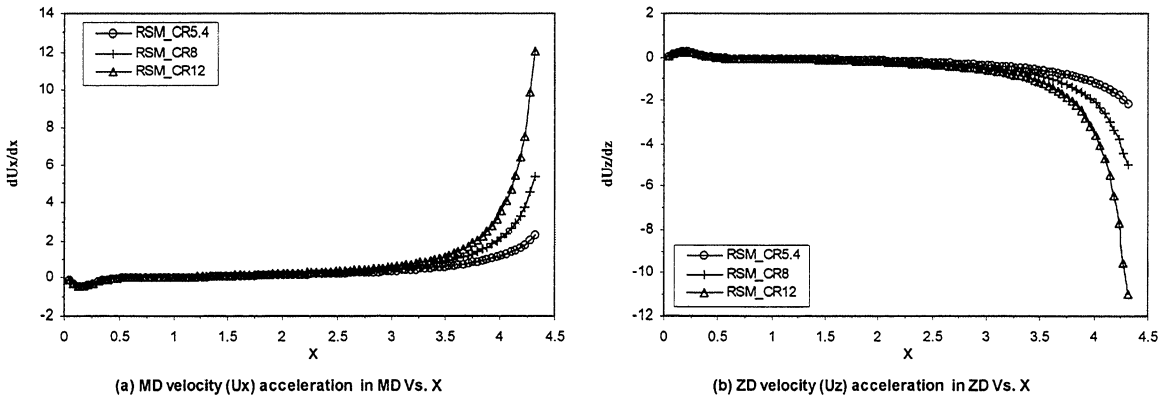

(a) MD velocity (Ux) acceleration in MD Vs. X

(b) ZD velocity (Uz) acceleration in ZD Vs. X

Figure 23 : Axial variation of MD and ZD velocity gradients in MD and ZD respectively

4.4. Effect of outlet boundary condition

As mentioned in § 3, zero traction boundary conditions have been applied at the outlet/slice of the headbox. This means that at the outlet, the jet is subject to zero normal and tangential stresses. This would be only applicable for fully developed channel and pipe flows. Hence, this might introduce some inaccuracy in the results at the slice, but we assume that its influence is limited only to a small region near the outlet. To

confirm this, plots of acceleration parameters have been presented in Fig.24. Acceleration parameter is defined in the literature [11-13] as

$$K = \frac{\nu}{U_m^{\,2}} \frac{dU_m}{dx} \tag{23}$$

For a linearly varying contraction, this should be a constant. In the current study, we define two parameters by slightly modifying the acceleration parameter (K) as

$$K_{md} = \frac{1}{\overline{u_x}^{\,2}} \frac{d\overline{u_x}}{dx} \tag{24}$$

$$K_{zd} = \frac{1}{\overline{u_z}^{\,2}} \frac{d\overline{u_z}}{dz} \tag{25}$$

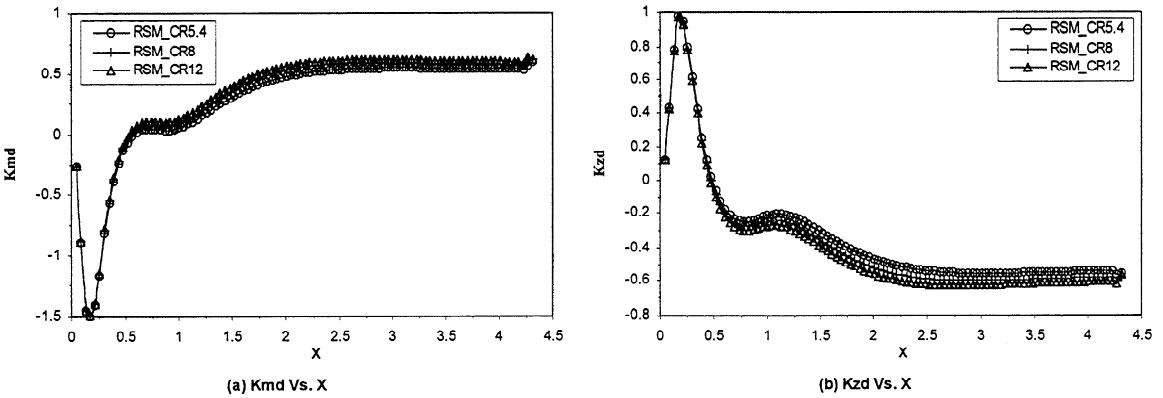

Figure 24 : Acceleration parameter variation for the three CR's

From Fig.24 it may be seen that the acceleration parameters in the later half of the nozzle remain fairly constant except at the outlet, where the outlet boundary condition influences the flow field. Also, this effect, being very local, may not influence the overall solution.

5. Conclusions

In this study, we have presented three-dimensional analysis of the jet interaction and the turbulent flow field in a headbox using both the RNG κ-ε model and the Reynolds Stress Model. The results obtained for three contraction ratios demonstrate the need for using the RSM in order to correctly analyze the Reynolds stress components. From a majority of the plots, it can be seen that the effect of sudden expansion of the jets and their interaction dominates in approximately the first half of the MD length of the headbox. The effect of contraction comes into picture in the later half of the headbox. Variation of some of the significant components of Reynolds stress tensor in the axial direction reveals that while the normal turbulent stress in the axial direction ($\rho\overline{u'^2}$) decreases along the contraction, the lateral normal stresses (namely, $\rho\overline{v'^2}$ and $\rho\overline{w'^2}$) increase in the contraction. $\rho\overline{u'v'}$ is the only significant shear stress component and this decreases in magnitude along the contraction. Thus the anisotropy in the turbulent stress tensor warrants the use of Reynolds Stress Model. A more detailed study of the relative strengths of the turbulent convective transport and the stress production terms is required to clearly understand the variations in the

turbulent stress tensor. Similarly, a study of the relative strengths of the mean convective terms and the turbulent stress terms is required to study the influence of the turbulence field on the fiber network orientation.

References

1. C.K.Aidun, Hydrodynamics of Streaks on the Forming Table, *TAPPI Journal*, **V** 80, **n** 8, **p**.155, 1997.
2. C.K.Aidun and A.E.Kovacs, Hydrodynamics of the Forming Section: Origin of Nonuniform Fiber Orientation, *TAPPI Journal*, **V** 78, **n** 11, **p**.97, 1995.
3. M.Ullmar and B.Norman, Observation of Fiber Orientation in a Headbox Nozzle at Low Consistency, *Engineering & Papermakers Conference*, **p**.865-873, 1997.
4. P.Tekriwal, Pressure Drop Calculations and Measurements in Converging-Diverging Nozzles, *Trans. ASME*, **p**.9, 1996.
5. G.V.Kudav and S.Ramamurthy, Flow Simulation in a Converging-Diverging Nozzle by Three Different Numerical Techniques, *Proceedings of the 46th National Conference on Fluid Power*, **p**.237, 1994.
6. J.C.Devine and PF.Peterson, Conjugate Heat Transfer in Converging-Diverging Nozzle Flow, *ASME Heat Transfer Div.*, **V** 245, **p**.29, 1993.
7. J.J.Brown, Navier-Stokes Nozzle Analysis Technique, *J. Propulsion Power*, **V** 3, **n** 4, **p**.334, 1987.
8. B.E.Launder, Laminarization of the Turbulent Boundary Layer in a Severe Pressure Gradient, *Trans. ASME J. Appl. Mech.*, **p**. 707, 1964.
9. P.M.Moretti and W.M.Kays, Heat Transfer to a Turbulent Boundary Layer with Varying Free-Stream Velocity and Varying Surface Temperature – an Experimental Study, *Int. J. Heat Mass Transfer*, **V** 8, **p**.1187, 1965.
10. Y.Senoo, The Boundary Layer on the End Wall of a Turbine Nozzle Cascade, *Trans. ASME*, **V** 80, **p**.1711, 1958.
11. M.A.Badri Narayanan, An Experimental Study of Reverse Transition in Two-Dimensional Channel flow, *J. Fluid Mech.*, **V** 31, **p**.609, 1968.
12. Y. Tanaka, and H.Yabuki, Laminarization and Reversion to Turbulence of Low Reynolds Number Flow Through a Converging to Constant Area Duct, *J. Fluids Engineering*, **V** 108, **p**.325, 1986.
13. M.Parsheh, A.A.Dahlkild and P.H.Alfredsson, *Relaminarization of a Turbulent Boundary Layer Subjected to Favorable Pressure Gradient in a Plane Contraction*, Technical Report, Department of Mechanics, Royal Institute of Technology, 1999.
14. S.V.Patankar, *Numerical Heat Transfer and Fluid Flow*, Hemisphere, New York, 1980.
15. J.O.Hinze, *Turbulence*, Second Edition, McGrawHill, 1975.
16. W.P.Jones and B.E.Launder, The Prediction of Laminarization with a Two-Equation Model of Turbulence, *Int. J. Heat Mass Transfer*, **V** 15, **p**.301, 1972.
17. A.Yakhot and S.A.Orszag, Renormalization Group Analysis of Turbulence: I. Basic Theory, *J. Sci. Comput.*, **V** 1, **n** 1, **p**.1, 1986.
18. D.Chowdhury, *Introduction to the Renormalization Group Method and Turbulence Modeling*, Fluent Inc., TM-107 (cross-reference), 1993.
19. B.E.Launder, Second Moment Closure: Present.. And Future?, *Int. J. Heat Fluid Flow*, **V** 10, **p**.282, 1989.
20. B.E.Launder, G.J.Reece and W.Rodi, Progress in the Development of a Reynolds Stress Turbulence Closure, *J. Fluid. Mech.*, **V** 68, **p**.537, 1975.
21. W.F.J.Sampers, A.P.G.G.Lamers and A.A.Van Steenhoven, Experimental and Numerical Analysis of a Turbulent Swirling Flow in a Tube, *Inst. Chem. Eng. Symp. Series*, **V** 2, **n** 129, **p**. 765, 1992.
22. S.Hirai, T.Takagi and T.Higashiya, Numerical Prediction of Flow Characteristics and Retardation of Mixing in a Turbulent Swirling Flow, *Int. J. Heat Mass Transfer*, **V** 23, **n** 1, **p**.121, 1989.